High-order simulation solving Navier-Stokes equations with Spalart–Allmaras turbulence model

High-order simulation solving Navier-Stokes equations with Spalart–Allmaras turbulence model

Li Yang[1, 2], Lianjie Yue[2, 3, *], Qifan Zhang[2, 3] and Xinyu Zhang[2, 3]

[1] School of Aerospace Engineering, Beijing Institute of Technology, Beijing, 100081, China
[2] State Key Laboratory of High Temperature Gas Dynamics, Institute of Mechanics, Chinese Academy of Sciences, Beijing, 100190, China
[3] School of Engineering Sciences, University of Chinese Academy of Sciences, Beijing, 100049, China

* Corresponding author: yuelj@imech.ac.cn

Abstract. The goal of this paper is to implement an accurate and robust solver for compressible Navier-Stokes equations coupled with the Spalart–Allmaras model, which possesses the capability of shock-capturing and predication of boundary layer and separated flow. In a given stencil width, a WENO-Z scheme equipped with Roe flux difference split method is used to calculate the inviscid flux, and central differencing scheme for the viscous terms are employed. The explicit Runge-Kutta is adopted for the temporal discretization. The simulation results of selected cases are given to verify the validation of the solver.

1. Introduction

Computational fluid dynamics (CFD) acts as an indispensable tool for widely industrial applications, such as aerospace, ocean engineering, weather environment, vehicle design and so on [1]. Up to now, direct numerical simulation (DNS), large eddy simulation (LES) and Reynolds averaged Navier-Stokes (RANS) simulation, are the dominant methods for the numerical solution of the turbulence flow [2]. With the consideration of computation requirement and efficiency, RANS techniques, which rely completely on modeling assumptions to represent turbulent characteristics, are the most common and popular method for the complex and large-scaled industrial problems. Additionally, detached-eddy simulation (DES) [3] has attracted increasing attention and would be the potential alternative for industries in future.

So far, most of the engineering applications is 2nd-order numerical accuracy solver, which is inadequate for certain engineering problems, such as hypersonic flow and detonation physics with the existence of strong shock wave. Then, weighted essentially non-oscillatory (WENO) schemes are attractive for their capability to treat the discontinuities and achieve the high order accuracy in the smooth regions, and amount of modified WENO schemes has been proposed till now. In the paper, the RANS equations combined with the one equation Spalart-Allmaras (SA) model without transition terms will be solved numerically. The 5th-order WENO-Z scheme for inviscid fluxes and 4th-order central differencing scheme for the viscous terms are employed, respectively.

2. Computation method

2.1. Governing equation

The two-dimensional Navier-Stokes equation is adopted in the study. The non-dimensional governing equations in curvilinear coordinates are summarized as follows [1].

$$J^{-1}\frac{\partial W}{\partial t}+J^{-1}\frac{\partial\left(\xi_x F+\xi_y G\right)}{\partial \xi}+J^{-1}\frac{\partial\left(\eta_x F+\eta_y G\right)}{\partial \eta}=\frac{J^{-1}}{\mathrm{Re}_\infty}\left(\frac{\partial\left(\xi_x F_v+\xi_y G_v\right)}{\partial \xi}+\frac{\partial\left(\eta_x F_v+\eta_y G_v\right)}{\partial \eta}\right), \quad (1)$$

where, W is the conservative solution vector, F and G are the convective terms, F_v and G_v are the diffusive terms:

$$\begin{aligned}
&\mathrm{W}=\left[\rho \quad \rho u \quad \rho v \quad \rho E \quad \rho Y\right]^T,\\
&F=\left[\rho u \quad \rho u^2+p \quad \rho uv \quad (\rho E+p)u \quad \rho uY\right]^T,\\
&G=\left[\rho v \quad \rho uv \quad \rho v^2+p \quad (\rho E+p)v \quad \rho vY\right]^T,\\
&F_{\mathrm{v}}=\left[0 \quad \tau_{xx} \quad \tau_{xy} \quad u\tau_{xx}+v\tau_{xy}+k_{eff}\frac{\partial T}{\partial x} \quad \rho D_{eff}\frac{\partial Y}{\partial x}\right]^T,\\
&G_{\mathrm{v}}=\left[0 \quad \tau_{yx} \quad \tau_{yy} \quad u\tau_{yx}+v\tau_{yy}+k_{eff}\frac{\partial T}{\partial y} \quad \rho D_{eff}\frac{\partial Y}{\partial y}\right]^T,
\end{aligned} \quad (2)$$

The non-dimensional strategy is similar to Blazek [1], and a coordinate transformation from (x, y) to (ξ, η) is processed with following grid metric:

$$J^{-1}=\frac{\partial(x,y)}{\partial(\xi,\eta)},\xi_x=J\cdot y_\eta,\xi_y=-J\cdot x_\eta,\eta_x=-J\cdot y_\xi,\eta_y=J\cdot x_\xi. \quad (3)$$

The variables have their usual meaning: ρ, u, v, E, p, and Y are density, x-direction velocity, y-direction velocity, total energy per mass, pressure and specie, respectively. The equation of state can be expressed as:

$$\mathrm{p}=(\gamma-1)\rho\left(E-\frac{u^2+v^2}{2}\right), \quad (4)$$

With the Bousinesq eddy viscosity assumption, the shear stresses (τ_{xx}, τ_{xy}, and τ_{yy}) are defined as follows:

$$\tau_{xx}=\frac{2}{3}\mu_{eff}\left(2\frac{\partial u}{\partial x}-\frac{\partial v}{\partial y}\right),\tau_{yy}=\frac{2}{3}\mu_{eff}\left(2\frac{\partial v}{\partial y}-\frac{\partial u}{\partial x}\right),\tau_{xy}=\tau_{yx}=\mu_{eff}\left(\frac{\partial u}{\partial y}+\frac{\partial v}{\partial x}\right), \quad (5)$$

In the above formulation, μ_{eff}, k_{eff} and D_{eff} are the effective viscosity, thermal conductivity and diffusion coefficients:

$$\mu_{eff}=\mu_l+\mu_t,k_{eff}=k_l+k_t \text{ with } k=\frac{\mu c_p}{\mathrm{Pr}},D_{eff}=D_l+D_t \text{ with } D=\frac{\mu}{\rho \mathrm{Sc}} \quad (6)$$

where, the subscripts l and t indicate laminar and turbulence parameters; Pr (Prandtl number) and Sc (Schimdt number) are 0.72, 0.9 and 0.5, 0.5 for laminar and turbulence flow, respectively; the laminar viscosity (molecular viscosity) μ_l can be computed with Sutherland law, and the turbulence viscosity μ_t is determined by the turbulence model:

$$\mu_t=\rho\tilde{\nu}f_{v1},f_{v1}=\frac{\chi^3}{\chi^3+c_{v1}^3},\chi=\frac{\tilde{\nu}}{\nu},\nu=\frac{\mu_l}{\rho}, \quad (7)$$

where, $\tilde{\nu}$ is the work variable of Spalart-Allmaras model, can be calculated by the following non-dimensional equation in conservative form without trip term (the related functions and the constants used in the turbulence model can be found in Ref. [4]):

$$\frac{\partial(\rho\tilde{\nu})}{\partial t}+\nabla\cdot(\rho\tilde{\nu}U)=\rho c_{b1}(1-f_{t2})\hat{S}\tilde{\nu}-\frac{1}{\mathrm{Re}_{\infty}}\rho(c_{w1}f_{w}-\frac{c_{b1}}{\kappa^{2}}f_{t2})(\frac{\tilde{\nu}}{d})^{2}$$
$$+\frac{1}{\mathrm{Re}_{\infty}\sigma}[\nabla\cdot((\mu_{l}+\rho\tilde{\nu})\nabla\tilde{\nu})+c_{b2}\rho(\nabla\tilde{\nu})^{2}-(\nu+\tilde{\nu})\nabla\rho\nabla\tilde{\nu}], \tag{8}$$

2.2. Numerical scheme

To compute inviscid fluxes, the WENO finite difference method is used to construct left and right states. The conservative variables reconstruction procedure of the 5th-order WENO-JS scheme can be expressed as [5]:

$$w_{i+1/2}^{WENO}=\sum_{m=0}^{2}\omega_{m}^{WENO}w_{i+1/2}^{m} \tag{9}$$

where $w_{i+1/2}^{m}$ is obtained by a second-order polynomial reconstruction of w on mth set of candidate stencils. ω_{m}^{WENO} is the weight factor, which is no-negative number and the sum of all weight factor is unity. In the paper, the WENO-Z method is adopted to decrease the numerical dissipation and improve the resolution efficiency of the WENO-JS scheme with new smoothness indicators [6]. To improve the robustness of WENO reconstruction, the conservative variables would transform to the local characteristic fields with a Roe average matric whose columns are right eigenvectors of Jacobian matrix, after WENO reconstruction is done in the characteristic fields, reconstruction variables transform back into physical space. Finally, the Riemann problem solver, Roe method, is employed to obtain inviscid fluxes [7].

The discretization of viscous terms is processed with fully conservative 4th-order accuracy finite central differencing scheme, and the viscous flux of the interface can be expressed:

$$(F_{v})_{i-1/2}=\frac{1}{24}\left(-\left(\bar{F}_{v}\right)_{i+1/2}+26\left(\bar{F}_{v}\right)_{i-1/2}-\left(\bar{F}_{v}\right)_{i-3/2}\right) \tag{10}$$

In order to achieve the satisfied order accuracy of viscous flux in a least stencil not wider than the total width of the WENO stencils, the terms used to compute $\bar{F}_{v}$, such as, the gradient of physical parameters and physical parameters at the interface, can be determined with given Taylor expansion coefficients, which a detail description can be found in Ref. [8,9]. It should be noted that the convective part of SA equation is fully coupled with that of Navier-Stokes equation and solved with WENO scheme. When the governing equations have been processed by spatial discretization, an ordinary differential equation is acquired and a 3rd-order explicit total-variation diminish(TVD) Runge-Kutta is adopted for the temporal discretization [5]. Additionally, the message passing interface (MPI) standard for message passing is implemented in the numerical simulations to improve the computational efficiency.

In the following section, several cases have been carried out to demonstrate the accuracy and robustness of our solver, and corresponding grid, reference value and experimental data are adopted from Ref. [10–12] in the current work.

3. Validation cases and results

3.1. Sod shock tube problem

The classic Sod shock tube problem is used to examine the shock-capturing ability of the solver for Euler equations. The initial condition is given as follow:

$$(\rho,u,p,\gamma)=\begin{cases}(1.0,0.75,1.0,\gamma_{1}) & 0.0<0<0.3\\(0.125,0.0,0.1,\gamma_{2}) & 0.3<0<1.0\end{cases} \tag{11}$$

where, for γ_1=γ_2=1.4, the corresponding condition is same with that Toro used [10], named 1-γ Sod problem; for γ_1=1.4 and γ_2=1.2, the case is a modified version to evaluate the shock-capturing ability for multi-species, called 2-γ Sod problem.

The numerical results of 1-γ Sod shock tube problem with various grid points against exact solution are depicted in Fig. 1, and its solution contains a right shock wave, a right contact discontinuity and a left expansion wave, which are zoomed, respectively. All used grid points can achieve qualitatively similar results, and convergence rates r_c based on density are listed in Table 1. It can be found that r_c is nearly 5/6, and r_c, at or below first order, is characteristic of all shock capturing schemes when applied to flows with embedded discontinuities [13].

Table 1. L1 density error norms and convergence rates rc for Sod shock tube problem

Δx	L_1	r_c
1/500	1.6504×10^{-3}	-
1/1000	8.1906×10^{-4}	1.0108
1/2000	4.3689×10^{-4}	0.9067

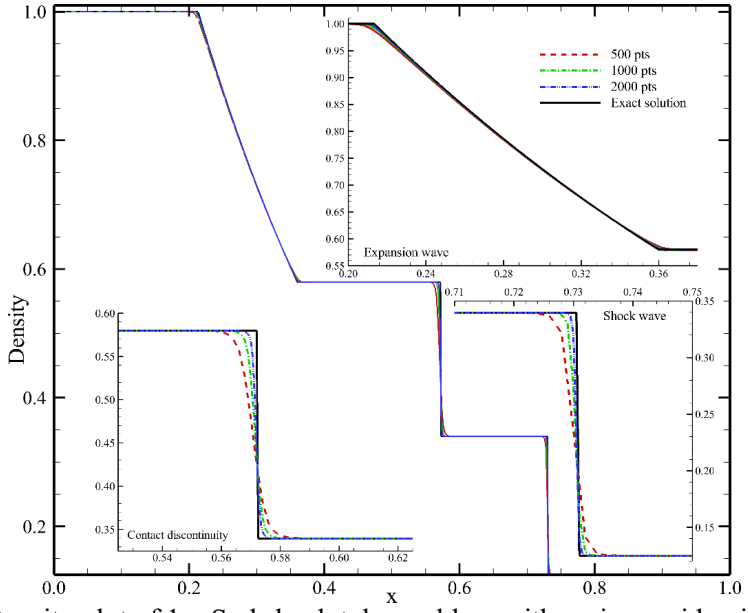

Figure 1. Density plot of 1-γ Sod shock tube problem with various grid points at t =0.2

As shown in Fig. 2, the computational solution compares well with the reference value [14] for 2-γ Sod shock tube problem. No oscillation of density and pressure exists near the interface of two species and shock wave, and the current solver can provide reliable results when applied to multi-species flows.

3.2. Laminar boundary layer

Primarily, a simple case of the laminar flow over an adiabatic flat plate at Mach number Ma_∞=0.2 and Reynolds number Re=1.3×10^6 based on the plate length [11], is employed to examine the Navier-Stokes equations solver without turbulence model. As shown in Fig. 3, the numerical result is comparable with the Blasius analytic solution.

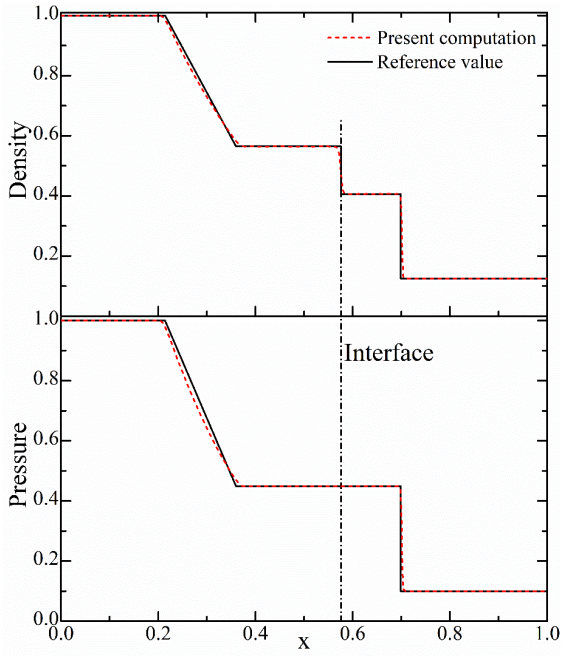

Figure 2. Density and pressure plot of 2-γ Sod shock tube problem with Δx=1/500 at t =0.2

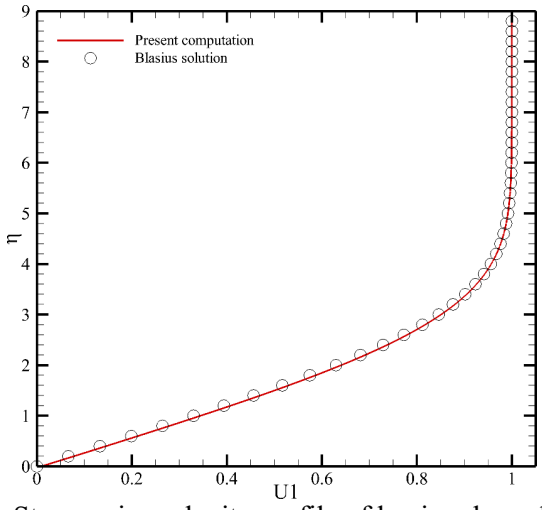

Figure 3. Streamwise velocity profile of laminar boundary layer

3.3. Turbulence boundary layer

To evaluate the RANS solver, a validation case that the turbulent boundary layer [11] is developed from supersonic flow over a flat plate at Ma_∞=4.512. The y^+ of the wall grid size at first layer is less than unity. The plots of velocity profile at x=1.79 ft and skin friction coefficient along plate are given in Fig 4, it can be found that the velocity profiles in sub-laminar layer and log-law zone agree well with the experimental value. Friction coefficient along plate have a similar tendency with experimental results only when Re_x>2.0×10^6 (where is fully turbulence flow), this may be due to that trip term is omitted in our turbulence model and it is arduous to predict this transition from laminar to turbulent well.

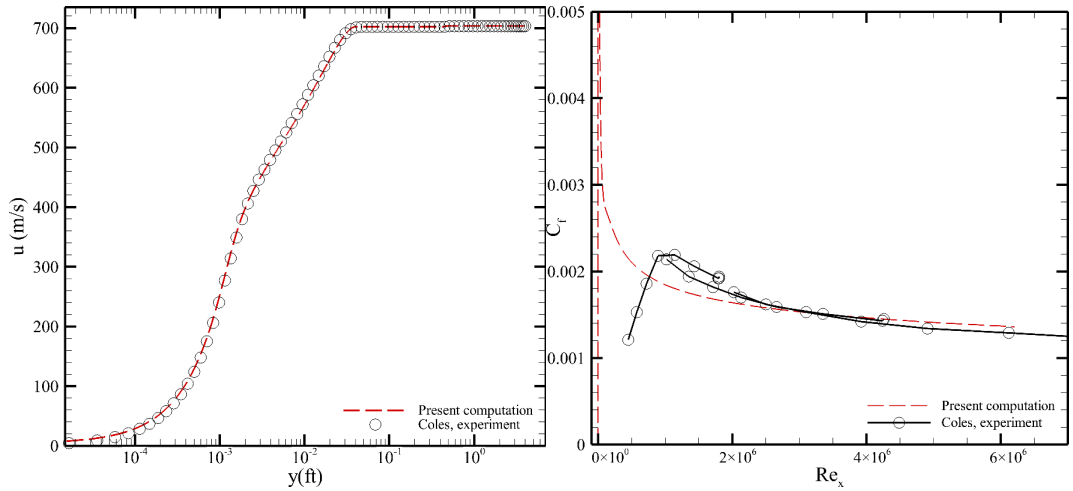

Figure 4. Streamwise velocity profile at x=1.79 ft (left) and skin friction coefficient of supersonic turbulence boundary layer (right).

3.4. Transonic RAE2822 airfoil

The results are presented for a transonic turbulent flow on a RAE2822 airfoil [11] at Ma_∞=0.729, Re=6.5×10^6, and angle-of-attack α=2.31 deg. The case aims at exploring the robustness of the RANS solver when combined with shock capturing. Fig. 5 shows the pressure coefficient distribution over the airfoil surface, that resembles the experimental results.

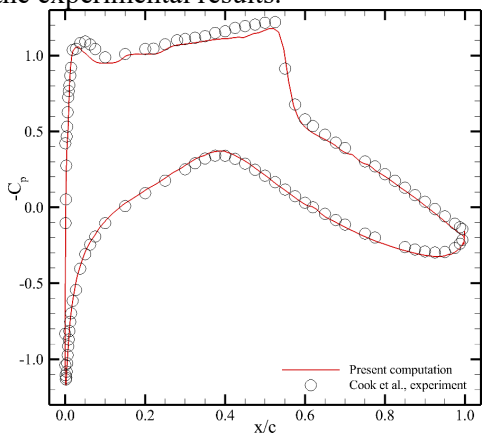

Figure 5. Pressure coefficient distribution over airfoil surface for turbulent transonic flow past RAE2822 foil

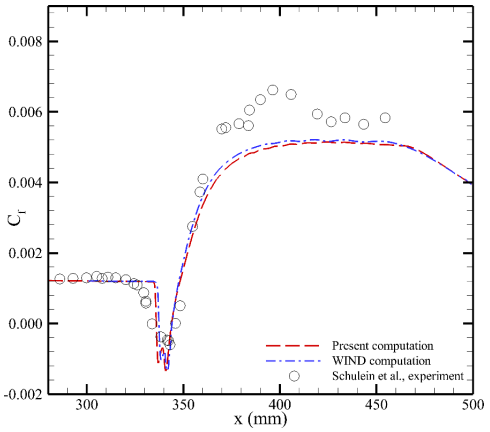

Figure 6. Skin friction coefficient of the flat plate for shock wave/boundary layer interaction designed by Schulein et al

3.5. Shock wave/boundary layer interaction

The validation case based on the experiment performed by Schulein et al., which uses a 10 deg wedge to create an oblique shock impinging on an opposite 500 mm long flat plate (isothermal wall, 300 K) to study a Mach 5 shock wave boundary-layer interaction [11]. Comparing the skin friction coefficient in Fig. 6, the present result is similar to that computed by the WIND code of NASA, which both underestimate the skin friction coefficient compared to the experimental data downstream of 360 mm, but the length-scale of separation zone agrees well with the experimental observation.

3.6. Separated flow of Wall-Mounted Hump

The focus of this case, wall-mounted hump separated flow (no plenum) with Ma_∞=0.1, Re=9.36×10^5, is to assess the ability of turbulence models to predict 2D separation from a smooth body as well as subsequent reattachment and boundary layer recovery [12]. As shown in Fig. 7, the separated flow can be visualized with the close-up velocity contour and streamline. The velocity profile at certain locations in/near the recirculation zone is plotted in Fig. 8, it can be seen that the boundary layer profiles compare well with measured values before the reattachment point. The length-scale of separation zone is slight larger than the experimental data as shown in Fig. 8, and a under prediction of skin friction coefficient also exists after the reattachment point. The simulation results of CFL3D and FUN3D with SA model have a similar tendency with our works, which are not given here for brevity. It manifests that the RANS simulation with SA model does not possess well ability to predict certain separated flows, and the DES based on SA model is need in the further application.

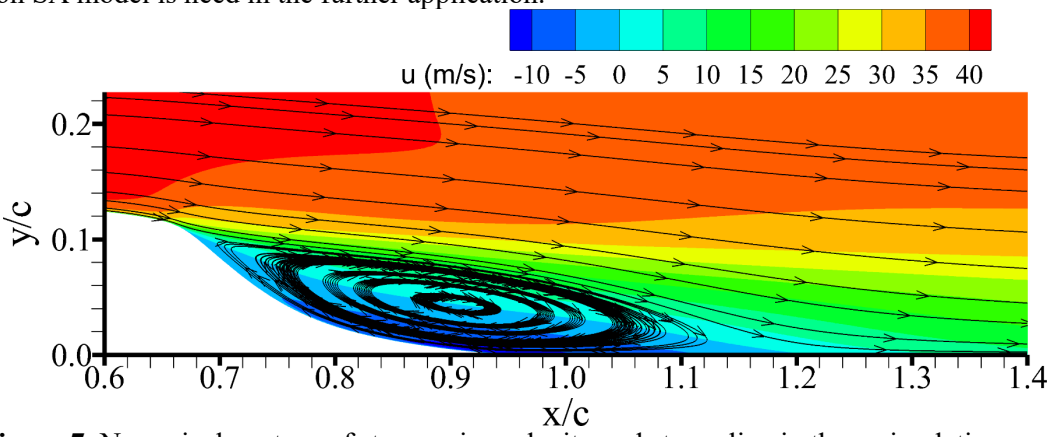

Figure 7. Numerical contour of streamwise velocity and streamline in the recirculation zone.

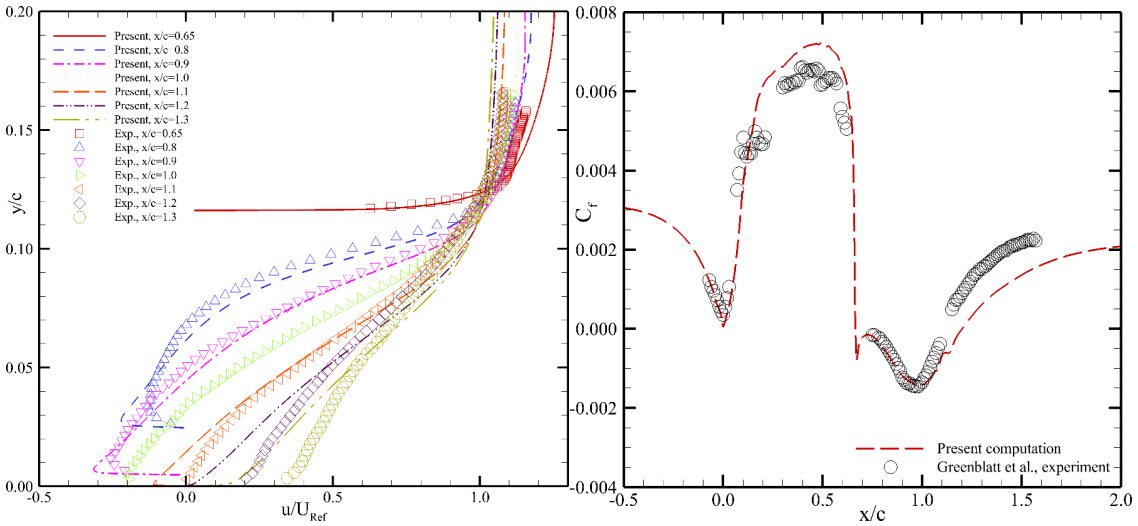

Figure 8. Streamwise velocity profile at different locations (left) and skin friction coefficient for wall-mounted hump separated flow (right).

4. Conclusion

In the current work, a high-order solver is developed for compressible Navier-Stokes equations embedded the SA model, which can capture shock wave and describe turbulence flow. For the spatial discretization, inviscid flux is computed with 5th-order WENO-Z method, and viscous flux is obtained by 4th-order central differencing scheme in the same stencil width of WENO. The SA turbulence model is fully coupled with the conservative equations and corresponding terms are solved in the same method. Then, the explicit TVD Runge-Kutta method manipulates the ordinary difference equations after the spatial discretization. A series of validation cases is calculated to demonstrate the ability of the solver in shock-capturing, laminar and turbulence boundary layer, and separated flow, and the numerical results show that the solver is accurate and robust, which can be applied to engineering issues in future.

Acknowledgments

The research is supported by the National Natural Science Foundation of China under grant numbers: 11672309 and 11472279.

References

[1] J. Blazek, Computational Fluid Dynamics: Principles and Applications, Third Edit, Butterworth-Heinemann, Oxford, 2015.
[2] K. Duraisamy, G. Iaccarino, H. Xiao, Turbulence Modeling in the Age of Data, Annu. Rev. Fluid Mech. 51 (2019) 357–377.
[3] P.R. Spalart, Detached-Eddy Simulation, Annu. Rev. Fluid Mech. 41 (2009) 181–202.
[4] P. Spalart, S. Allmaras, A one-equation turbulence model for aerodynamic flows, in: 30th Aerosp. Sci. Meet. Exhib., 1992.
[5] G.S. Jiang, C.W. Shu, Efficient implementation of weighted ENO schemes, J. Comput. Phys. 126 (1996) 202–228.
[6] F. Acker, R.B.R. Borges, B. Costa, An improved WENO-Z scheme, J. Comput. Phys. 313 (2016) 726–753.
[7] P.L. Roe, Approximate Riemann Solvers, Parameter Vectors, and Difference Schemes, J. Comput. Phys. 135 (1997) 250–258.
[8] Y. Shen, B. Wang, G. Zha, Implicit WENO Scheme and High Order Viscous Formulas for Compressible Flows, in: 25th AIAA Appl. Aerodyn. Conf., 2007: pp. 1756–1773.
[9] Z.-S. Sun, Y.-X. Ren, S.-Y. Zhang, Y.-C. Yang, High-resolution finite difference schemes using curvilinear coordinate grids for DNS of compressible turbulent flow over wavy walls, Comput. Fluids. 45 (2011) 84–91.
[10] E.F. Toro, Riemann Solvers and Numerical Methods for Fluid Dynamics, Springer Berlin Heidelberg, Berlin, Heidelberg, 2009.
[11] Information on https://www.grc.nasa.gov/WWW/wind/valid/archive.html.
[12] Information on https://www.turbmodels.larc.nasa.gov/index.html.
[13] A.K. Henrick, T.D. Aslam, J.M. Powers, Mapped weighted essentially non-oscillatory schemes: Achieving optimal order near critical points, J. Comput. Phys. 207 (2005) 542–567.
[14] V.K. Tritschler, X.Y. Hu, S. Hickel, N.A. Adams, Numerical simulation of a Richtmyer-Meshkov instability with an adaptive central-upwind sixth-order WENO scheme, Phys. Scr. (2013) 14016.